Phenomenology of the minimal inverse-seesaw model with Abelian flavour symmetries

Henrique Pedro Fernandes de Noronha Brito Câmara
Under supervision of Filipe Rafael Joaquim and Ricardo González Felipe
Departamento de Física and CFTP, Instituto Superior Técnico, Lisboa, Portugal
(Dated: December 2020)

In this work we study the phenomenology of the minimal inverse-seesaw model, which is composed of two "right-handed neutrinos" and two sterile singlet fermions, besides the Standard Model particle content. The model is supplemented with Abelian flavour symmetries to ensure maximal predictability and establish the most restrictive flavour patterns which can be realised by those symmetries. This setup requires adding an extra scalar doublet and two complex scalar singlets to the Standard Model, paving the way to implement spontaneous CP violation. It is shown that such CP-violating effects can be successfully communicated to the lepton sector through couplings of the scalar singlets to the new sterile fermions. The Majorana and Dirac CP phases turn out to be related, and the active-sterile neutrino mixing is determined by the active neutrino masses, mixing angles and CP phases. We investigate the constraints imposed on the model by the current experimental limits as well as future projected sensitivities on charged lepton flavour-violating decays and searches sensitive to the presence of heavy sterile neutrinos.
Keywords: Inverse seesaw; texture zeros; Abelian flavour symmetries; spontaneous CP violation; lepton flavour violation.

I. INTRODUCTION

The Standard Model (SM) [1–3] is one of the major achievements of particle physics. However, the discovery of neutrino oscillations [4, 5] has established that neutrinos are massive particles and that there is lepton mixing, which must be accounted for in extensions of the SM. From a theoretical perspective, the seesaw mechanism [6–14] offers an elegant framework for the explanation of the origin of neutrino masses and mixing.

As opposed to the canonical type-I seesaw, where very heavy "right-handed" (RH) neutrinos or tiny Yukawa couplings are required to generate small neutrino masses, in the so-called inverse seesaw (ISS) [12–14] neutrino mass suppression is triggered by small lepton-number violating (LNV) mass parameters. In this case, small Majorana neutrino masses can be generated with RH neutrino masses at the TeV scale (or below) and $\mathcal{O}(1)$ Yukawa coupling parameters. As a result, the mixing between the (active) light neutrinos and the new (sterile) states can be sizeable for sterile neutrino masses lying not far from the electroweak scale. The presence of new neutral fermions interacting with SM leptons and gauge bosons motivates phenomenological studies beyond the SM, making the ISS a perfect theoretical framework to guide new physics probes.

A challenging issue in particle physics is the lack of a principle to explain the flavour structure of the SM, i.e., the observed fermion mass spectra and mixing patterns. This *flavour puzzle* provides a strong motivation for building models with additional particle content and extended symmetries. One of the simplest approaches consists on the implementation of texture zeros in the Yukawa coupling and mass matrices, imposed by continuous U(1) and/or discrete $\mathbb{Z}_N$ transformations [15, 16]. In the SM extended with RH neutrinos, the realisation of texture zeros with such symmetries is not compatible with data since, in general, they lead to massless charged leptons and/or vanishing lepton mixing angles [16, 17]. Thus, enlarging the Higgs sector is a viable solution to surmount this difficulty, being the two-Higgs doublet model (2HDM) [18] the most economical one.

Inspired by the above ideas, in this work we consider the ISS(2,2), which is the minimal setup composed of two RH neutrinos and two sterile singlet fermions [19], within the 2HDM supplemented with Abelian symmetries to ensure maximal predictability, i.e., to impose the most constraining flavour structure, so that the charged-lepton masses and neutrino data can be accommodated, while fulfilling all phenomenological constraints, namely the ones on charged lepton flavour-violating (cLFV) processes. This can be realised by adding to the SM another scalar doublet and two complex scalar singlets which, upon spontaneous symmetry breaking (SSB), generate all relevant mass terms required to implement the ISS(2,2). The work presented here follows closely Ref. [20].

II. INVERSE SEESAW MECHANISM

The ISS mechanism can be implemented by extending the SM particle content with n_R RH neutrinos ν_R and n_s sterile fermion singlets s, leading to what we denote as ISS(n_R, n_s). In this framework, the generic mass Lagrangian for leptons is given in the flavour basis by

$$-\mathcal{L}_{\text{mass}} = \overline{e_L}\mathbf{M}_\ell\, e_R + \frac{1}{2}\,\overline{N_L^c}\,\boldsymbol{\mathcal{M}}\,N_L + \text{H.c.}\ ,$$
$$\boldsymbol{\mathcal{M}} = \begin{pmatrix} 0 & \mathbf{M}_D^* & 0 \\ \mathbf{M}_D^\dagger & 0 & \mathbf{M}_R \\ 0 & \mathbf{M}_R^T & \mathbf{M}_s \end{pmatrix}\ , \tag{1}$$

where $\mathbf{M}_\ell$ is the 3×3 charged-lepton mass matrix and $N_L = (\nu_L, \nu_R^c, s)^T$ of dimension $n_f = 3 + n_R + n_s$

with $\nu_L = (\nu_{eL}, \nu_{\mu L}, \nu_{\tau L})^T$, $\nu_R = (\nu_{R1}, \dots, \nu_{Rn_R})^T$, $s = (s_1, \dots, s_{n_s})^T$. For a fermion field ψ we have $\psi^c \equiv C\overline{\psi}^T$ with C denoting the charge conjugation matrix. Furthermore, the full $n_f \times n_f$ neutrino mass matrix $\boldsymbol{\mathcal{M}}$ is composed by $\mathbf{M}_D$ a $3 \times n_R$ Dirac-type mass matrix, $\mathbf{M}_R$ a $n_R \times n_s$ matrix, and $\mathbf{M}_s$ a LNV $n_s \times n_s$ Majorana mass matrix. The latter can be naturally small in the 't Hooft [21] sense, since if we set this matrix to zero lepton number conservation is restored.

The charged-lepton mass matrix is bidiagonalised through the unitary transformations $e_{L,R} \to \mathbf{V}_{L,R}\, e_{L,R}$,

$$\mathbf{V}_L^\dagger \mathbf{M}_\ell \mathbf{V}_R = \mathbf{D}_\ell = \mathrm{diag}\,(m_e, m_\mu, m_\tau)\,, \tag{2}$$

with $m_{e,\mu,\tau}$ denoting the physical charged-lepton masses. For a given $\mathbf{M}_\ell$, $\mathbf{V}_{L,R}$ are determined by diagonalising the Hermitian matrices $\mathbf{H}_\ell = \mathbf{M}_\ell \mathbf{M}_\ell^\dagger$ and $\mathbf{H}'_\ell = \mathbf{M}_\ell^\dagger \mathbf{M}_\ell$.

The weak-basis states N_L are related to the mass eigenstates $(\nu_1, ..., \nu_{n_f})^T$ by a $n_f \times n_f$ unitary matrix $\boldsymbol{\mathcal{U}}$,

$$N_L = \boldsymbol{\mathcal{U}}\, (\nu_1, \dots\ , \nu_{n_f})_L^T\,, \tag{3}$$

such that $\boldsymbol{\mathcal{M}}$ is diagonalised as

$$\boldsymbol{\mathcal{U}}^T \boldsymbol{\mathcal{M}}\, \boldsymbol{\mathcal{U}} = \boldsymbol{\mathcal{D}}_\nu = \mathrm{diag}\,(m_1, \dots\ , m_{n_f})\,, \tag{4}$$

where $m_{1,\dots,n_f}$ are the n_f (real and positive) Majorana neutrino masses. In the ISS approximation limit ($\mathbf{M}_s, \mathbf{M}_D \ll \mathbf{M}_R$), the neutrino mass matrix $\boldsymbol{\mathcal{M}}$ of Eq. (1) can be block-diagonalised by writing

$$\boldsymbol{\mathcal{M}} = \left(\begin{array}{c|cc} 0 & \mathbf{M}_D^* & 0 \\ \hline \mathbf{M}_D^\dagger & 0 & \mathbf{M}_R \\ 0 & \mathbf{M}_R^T & \mathbf{M}_s \end{array}\right) \equiv \begin{pmatrix} 0 & \mathbf{M}'_D \\ \mathbf{M}'^T_D & \mathbf{M}'_R \end{pmatrix}. \tag{5}$$

The full unitary matrix $\boldsymbol{\mathcal{U}}$ of Eq. (4) can then be parameterised as [22]

$$\boldsymbol{\mathcal{U}} = \begin{pmatrix} \sqrt{\mathbb{1} - \mathbf{F}\mathbf{F}^\dagger} & \mathbf{F} \\ -\mathbf{F}^\dagger & \sqrt{\mathbb{1} - \mathbf{F}^\dagger\mathbf{F}} \end{pmatrix} \begin{pmatrix} \mathbf{U}_\nu & 0 \\ 0 & \mathbf{U}_s \end{pmatrix}, \tag{6}$$

where $\mathbf{F}$ is a $3 \times (n_R + n_s)$ matrix given at first order in the seesaw approximation by

$$\mathbf{F} \simeq \mathbf{M}'^*_D\, (\mathbf{M}'^*_R)^{-1} \simeq \left(0,\ \mathbf{M}_D (\mathbf{M}_R^\dagger)^{-1}\right). \tag{7}$$

The above block-diagonalisation procedure leads to the $(n_R + n_s) \times (n_R + n_s)$ mass matrix $\mathbf{M}_{\rm heavy} \simeq \mathbf{M}'_R$, diagonalised by $\mathbf{U}_s$ and yielding $n_R + n_s$ heavy neutrinos. Furthermore, we obtain the 3×3 effective light-neutrino mass matrix

$$-\mathbf{M}_{\rm eff} = \mathbf{F}^* \mathbf{M}'_R \mathbf{F}^\dagger = \mathbf{M}_D^*\, \left(\mathbf{M}_R\, \mathbf{M}_s^{-1} \mathbf{M}_R^T\right)^{-1} \mathbf{M}_D^\dagger\,, \tag{8}$$

which can be diagonalised through a unitary rotation of the active neutrino fields, $\nu_L \to \mathbf{U}_\nu\, \nu_L$, satisfying

$$\mathbf{U}_\nu^T\, \mathbf{M}_{\rm eff}\, \mathbf{U}_\nu = \mathbf{D}_\nu = \mathrm{diag}\,(\tilde{m}_1, \tilde{m}_2, \tilde{m}_3)\,, \tag{9}$$

where $\tilde{m}_{1,2,3}$ are the real and positive light neutrino masses in the ISS approximation. The unitary matrix $\mathbf{U}_\nu$ is obtained from the diagonalisation of the Hermitian matrix $\mathbf{H}_{\rm eff} = \mathbf{M}_{\rm eff} \mathbf{M}_{\rm eff}^\dagger$. This yields the unitary lepton mixing matrix

$$\mathbf{U}' = \mathbf{V}_L^\dagger \mathbf{U}_\nu\,. \tag{10}$$

In general, for massive Majorana neutrinos, $\mathbf{U}'$ can be parameterised by three mixing angles θ_{12}, θ_{23}, and θ_{13}, and three CP-violating phases: the Dirac-type phase δ and two Majorana-type phases α_{21} and α_{31} [23],

$$\mathbf{U}' = \begin{pmatrix} c_{12}c_{13} & s_{12}c_{13} & s_{13} \\ -s_{12}c_{23} - c_{12}s_{23}s_{13}e^{i\delta} & c_{12}c_{23} - s_{12}s_{23}s_{13}e^{i\delta} & s_{23}c_{13}e^{i\delta} \\ s_{12}s_{23} - c_{12}c_{23}s_{13}e^{i\delta} & -c_{12}s_{23} - s_{12}c_{23}s_{13}e^{i\delta} & c_{23}c_{13}e^{i\delta} \end{pmatrix} \begin{pmatrix} 1 & 0 & 0 \\ 0 & e^{i\alpha_{21}} & 0 \\ 0 & 0 & e^{i\alpha_{31}} \end{pmatrix}, \tag{11}$$

where $c_{ij} \equiv \cos\theta_{ij}$ and $s_{ij} \equiv \sin\theta_{ij}$. We present in Table I the results obtained from the most recent global fit of neutrino oscillation parameters [24]. Note that $\Delta m^2_{21} = m_2^2 - m_1^2$, $\Delta m^2_{31} = m_3^2 - m_1^2$. Both mass orderings are considered: normal ordering (NO) where $m_1 < m_2 < m_3$, and inverted ordering (IO) where $m_3 < m_1 < m_2$. Notice also that the lepton sector is described by a total of twelve parameters: three charged lepton masses, three light neutrino masses, three mixing angles and three phases. In the case of a massless neutrino there is only one physical Majorana phase and, thus, the total number of physical parameters in the lepton sector is reduced to ten.

Consider the rectangular $3 \times n_f$ matrix $\mathbf{W}_{\alpha j} \equiv \boldsymbol{\mathcal{U}}_{\alpha j}$ ($\alpha = e, \mu, \tau$, $j = 1, \dots, n_f$) which, according to Eq. (6), can be decomposed in the form

$$\mathbf{W} = (\sqrt{\mathbb{1} - \mathbf{F}\mathbf{F}^\dagger}\, \mathbf{U}_\nu\,,\, \mathbf{F}\mathbf{U}_s) \equiv (\mathbf{W}_\nu, \mathbf{W}_s)\,, \tag{12}$$

where $\mathbf{W}_\nu$ and $\mathbf{W}_s$ are 3×3 and $3 \times (n_R + n_s)$ matrices, respectively. Due to the additional fermion states, active-neutrino mixing is determined by the non-unitary matrix

$$\mathbf{U} = \mathbf{V}_L^\dagger \mathbf{W}_\nu = (\mathbb{1} - \boldsymbol{\eta})\, \mathbf{U}', \tag{13}$$

where $\mathbf{U}'$ is the unitary mixing matrix given in Eq. (10) and $\boldsymbol{\eta}$ is an Hermitian matrix encoding deviations from unitarity of $\mathbf{U}$. Furthermore, $\mathbf{V}_L^\dagger \mathbf{W}_s$ defines the mixing

Parameter	Best Fit $\pm 1\sigma$	3σ range
$\theta_{12}(^\circ)$	34.3 ± 1.0	$31.4 \to 37.4$
$\theta_{23}(^\circ)$[NO]	$48.79^{+0.93}_{-1.25}$	$41.63 \to 51.32$
$\theta_{23}(^\circ)$[IO]	$48.79^{+1.04}_{-1.30}$	$41.88 \to 51.30$
$\theta_{13}(^\circ)$[NO]	$8.58^{+0.11}_{-0.15}$	$8.16 \to 8.94$
$\theta_{13}(^\circ)$[IO]	$8.63^{+0.11}_{-0.15}$	$8.21 \to 8.99$
$\delta(^\circ)$[NO]	216^{+41}_{-25}	$144 \to 360$
$\delta(^\circ)$[IO]	277^{+23}_{-24}	$205 \to 342$
Δm^2_{21} $(\times 10^{-5}$ eV$^2)$	$7.50^{+0.22}_{-0.20}$	$6.94 \to 8.14$
$\lvert\Delta m^2_{31}\rvert$ $(\times 10^{-3}$ eV$^2)$ [NO]	$2.56^{+0.03}_{-0.04}$	$2.46 \to 2.65$
$\lvert\Delta m^2_{31}\rvert$ $(\times 10^{-3}$ eV$^2)$ [IO]	2.46 ± 0.03	$2.37 \to 2.55$

TABLE I. Current neutrino data obtained from the global fit of three flavour oscillation parameters [24].

between the three active neutrinos and the n_R+n_s sterile states in the physical charged-lepton basis, which at first order in $\mathbf{F}$ is

$$\mathbf{V}_L^\dagger \mathbf{W}_s = \mathbf{V}_L^\dagger \mathbf{F} \mathbf{U}_s \simeq \mathbf{V}_L^\dagger \big(0,\ \mathbf{M}_D (\mathbf{M}_R^\dagger)^{-1}\big)\mathbf{U}_s. \quad (14)$$

The parameters $\boldsymbol{\eta}_{\alpha\beta}$ encoding deviations from unitarity can be expressed solely in terms of the active-sterile mixing through the relations

$$\boldsymbol{\eta}_{\alpha\beta} = \frac{1}{2}\sum_{j=4}^{n_f} \mathbf{B}_{\alpha j}\mathbf{B}^*_{\beta j}\ ,\ \mathbf{B}_{\alpha j} = \sum_{k=1}^{3} (\mathbf{V}_L^*)_{k\alpha}\mathbf{W}_{kj}. \quad (15)$$

The mixing between the light and sterile neutrinos is also given by the matrix elements $\mathbf{B}_{\alpha j}$ for $\alpha = e, \mu, \tau$ and $j = 4, \ldots, n_f$.

III. MAXIMALLY-RESTRICTIVE TEXTURES FOR LEPTONS

In this section, we identify the maximally-restrictive textures for the set of matrices $(\mathbf{M}_\ell, \mathbf{M}_D, \mathbf{M}_R, \mathbf{M}_s)$ compatible with neutrino oscillation data within the minimal ISS(2,2) framework, where $n_R = n_s = 2$ and $n_f = 7$. Our texture-zero analysis is performed assuming the seesaw approximation given in Eq. (8). The identification of the compatible textures is based on a standard χ^2-analysis, using the function

$$\chi^2(x) = \sum_i \frac{\left[\mathcal{P}_i(x) - \mathcal{O}_i\right]^2}{\sigma_i^2}, \quad (16)$$

where x denotes the input parameters, i.e., the matrix elements of $\mathbf{M}_\ell$, $\mathbf{M}_D$, $\mathbf{M}_R$ and $\mathbf{M}_s$; $\mathcal{P}_i(x)$ is the model prediction for a given observable with best-fit (b.f.) value $\mathcal{O}_i$, and σ_i denotes its 1σ experimental uncertainty. In our search for viable sets $(\mathbf{M}_\ell, \mathbf{M}_D, \mathbf{M}_R, \mathbf{M}_s)$, we require the charged-lepton masses to be at their central values [25], such that the χ^2-function is minimised only with respect to the six remaining neutrino oscillation observables, using the current data reported in Table I [24]. Notice that, in the ISS(2,2) framework, there is always a massless neutrino ($\tilde{m}_1 = 0$ for NO or $\tilde{m}_3 = 0$ for IO).

$\mathbf{M}_\ell = 6^\ell$			$\mathbf{M}_\ell = 5^\ell_1$			$\mathbf{M}_\ell = 4^\ell_{1,2,3}$		
$\mathbf{M}_D$	$\mathbf{M}_R$	$\mathbf{M}_s$	$\mathbf{M}_D$	$\mathbf{M}_R$	$\mathbf{M}_s$	$\mathbf{M}_D$	$\mathbf{M}_R$	$\mathbf{M}_s$
T_1	T_{14}	T_{23}	T_{13}	T_{14}	T_{23}	T_{124}	T_{14}	T_{23}
T_4	T_{14}	T_{23}	T_{14}	T_{14}	T_{23}	T_{125}	T_{14}	T_{23}
T_5	T_{14}	T_{23}	T_{16}	T_{14}	T_{23}	T_{134}	T_{14}	T_{23}
T_{14}	T_1	T_{23}	T_{35}	T_{14}	T_{23}	T_{136}	T_{14}	T_{23}
T_{16}	T_1	T_{23}	T_{45}	T_{14}	T_{23}	T_{145}	T_{14}	T_{23}
T_{23}	T_1	T_{23}				T_{146}	T_{14}	T_{23}
T_{25}	T_1	T_{23}				T_{156}	T_{14}	T_{23}
T_{36}	T_1	T_{23}				T_{345}	T_{14}	T_{23}
T_{45}	T_1	T_{23}				T_{456}	T_{14}	T_{23}

TABLE II. Maximally-restrictive texture sets for $\mathbf{M}_\ell = 6^\ell$ (left), 5^ℓ_1 (centre) and $4^\ell_{1,2,3}$ (right).

$$4^\ell_1 \sim \begin{pmatrix} 0 & 0 & \times \\ 0 & \times & 0 \\ \times & \times & \times \end{pmatrix}\ 4^\ell_2 \sim \begin{pmatrix} 0 & 0 & \times \\ 0 & \times & \times \\ \times & 0 & \times \end{pmatrix}\ 4^\ell_3 \sim \begin{pmatrix} 0 & 0 & \times \\ 0 & \times & \times \\ \times & \times & 0 \end{pmatrix}$$

$$5^\ell_1 \sim \begin{pmatrix} 0 & 0 & \times \\ 0 & \times & 0 \\ \times & 0 & \times \end{pmatrix}\ 6^\ell \sim \begin{pmatrix} \times & 0 & 0 \\ 0 & \times & 0 \\ 0 & 0 & \times \end{pmatrix}$$

TABLE III. Textures for the charged-lepton mass matrix $\mathbf{M}_\ell$.

For a given set of input matrices, we consider compatibility with data if the deviation of each neutrino observable from its experimental value is at most 3σ at the χ^2-minimum [15, 16]. If this is the case, we also test the compatibility of the textures at 1σ. For the sake of simplicity, we shall use the following sequential notation to label the position of the matrix elements of a given 3×2 and 2×2 texture T, respectively,

$$\begin{pmatrix} 1 & 2 \\ 3 & 4 \\ 5 & 6 \end{pmatrix}, \quad \begin{pmatrix} 1 & 2 \\ 3 & 4 \end{pmatrix}, \quad (17)$$

where we denote the position of any vanishing element labelled i with a subscript, i.e., T_i.

The maximally-restrictive texture zero sets $(\mathbf{M}_\ell, \mathbf{M}_D, \mathbf{M}_R, \mathbf{M}_s)$ compatible with oscillation data for NO are presented in Table II. It turns out that these sets of matrices are also viable for IO. Moreover, all the sets are compatible with data at 1σ. The labelling used for the $\mathbf{M}_\ell$ matrix in Table III follows Ref. [26].

IV. ABELIAN SYMMETRY REALISATION OF COMPATIBLE TEXTURES

We start this section by specifying the scalar sector of the model. As mentioned before, our minimal setup will require the presence of at least two Higgs doublets Φ_a $(a = 1, 2)$. Furthermore, to avoid bare mass terms in the Lagrangian, we also add two complex scalar fields S_a $(a = 1, 2)$, so that $\mathbf{M}_s$ and $\mathbf{M}_R$ are dynamically generated through couplings of S_1 and S_2 with $\overline{s^c} s$ and $\overline{\nu_R}\, s$, respectively.

$\mathbf{M}_\ell$	$\mathbf{Y}^1_\ell$	$\mathbf{Y}^2_\ell$
4^ℓ_3	$\begin{pmatrix}0&0&\times\\0&\times&0\\\times&0&0\end{pmatrix}$	$\begin{pmatrix}0&0&0\\0&0&\times\\0&\times&0\end{pmatrix}$
$5^\ell_{1,\mathrm{I}}$	$\begin{pmatrix}0&0&\times\\0&0&0\\\times&0&0\end{pmatrix}$	$\begin{pmatrix}0&0&0\\0&\times&0\\0&0&\times\end{pmatrix}$
$5^\ell_{1,\mathrm{II}}$	$\begin{pmatrix}0&0&\times\\0&\times&0\\\times&0&0\end{pmatrix}$	$\begin{pmatrix}0&0&0\\0&0&0\\0&0&\times\end{pmatrix}$

$\mathbf{M}_R$	$\mathbf{Y}_R$
T_{14}	$\begin{pmatrix}0&\times\\\times&0\end{pmatrix}$

$\mathbf{M}_s$	$\mathbf{Y}^1_s$	$\mathbf{Y}^2_s$
T_{23}	$\begin{pmatrix}\times&0\\0&0\end{pmatrix}$	$\begin{pmatrix}0&0\\0&\times\end{pmatrix}$

$\mathbf{M}_D$	$\mathbf{Y}^1_D$	$\mathbf{Y}^2_D$
T_{45}	$\begin{pmatrix}\times&0\\0&0\\0&\times\end{pmatrix}$	$\begin{pmatrix}0&\times\\\times&0\\0&0\end{pmatrix}$
T_{124}	$\begin{pmatrix}0&0\\0&0\\\times&0\end{pmatrix}$	$\begin{pmatrix}0&0\\\times&0\\0&\times\end{pmatrix}$
T_{456}	$\begin{pmatrix}0&\times\\\times&0\\0&0\end{pmatrix}$	$\begin{pmatrix}\times&0\\0&0\\0&0\end{pmatrix}$
$\mathrm{T}_{136,\mathrm{I}}$	$\begin{pmatrix}0&0\\0&\times\\0&0\end{pmatrix}$	$\begin{pmatrix}0&\times\\0&0\\\times&0\end{pmatrix}$
$\mathrm{T}_{136,\mathrm{II}}$	$\begin{pmatrix}0&\times\\0&0\\0&0\end{pmatrix}$	$\begin{pmatrix}0&0\\0&\times\\\times&0\end{pmatrix}$
$\mathrm{T}_{146,\mathrm{I}}$	$\begin{pmatrix}0&\times\\0&0\\\times&0\end{pmatrix}$	$\begin{pmatrix}0&0\\\times&0\\0&0\end{pmatrix}$
$\mathrm{T}_{146,\mathrm{II}}$	$\begin{pmatrix}0&\times\\\times&0\\0&0\end{pmatrix}$	$\begin{pmatrix}0&0\\0&0\\\times&0\end{pmatrix}$

TABLE IV. Decomposition of mass matrices into the Yukawa textures according to Eq. (18).

The Yukawa Lagrangian relevant for our work is

$$\begin{aligned}-\mathcal{L}_{\text{Yuk.}} &= \overline{\ell_L}\mathbf{Y}^a_\ell\Phi_a e_R + \overline{\ell_L}\mathbf{Y}^a_D\tilde{\Phi}_a\nu_R \\ &+ \frac{1}{2}\,\overline{s^c}\left(\mathbf{Y}^1_s S_1 + \mathbf{Y}^2_s S_1^*\right)s \\ &+ \overline{\nu_R}\left(\mathbf{Y}^1_R S_2 + \mathbf{Y}^2_R S_2^*\right)s + \text{H.c.},\end{aligned} \tag{18}$$

where the sum over a is implicit. Upon SSB, the scalar fields acquire non-zero vacuum expectation values (VEV)

$$\begin{aligned}&\langle\phi_1^0\rangle = v\cos\beta\ ,\ \langle\phi_2^0\rangle = v\sin\beta\ ,\ \tan\beta = \frac{v_2}{v_1}\\ &\langle S_1\rangle = u_1 e^{i\xi}\ ,\ \langle S_2\rangle = u_2,\end{aligned} \tag{19}$$

and the above Yukawa interactions yield the generic mass Lagrangian of Eq. (1) for the ISS(2,2).

To identify which of the maximally-restrictive texture sets compatible with neutrino data (see previous section) can be realised by imposing discrete or continuous Abelian symmetries, we apply two complementary methods, namely the canonical [27] and Smith normal form (SNF) [28] methods. We follow closely the methodology employed in Refs. [15, 16].

In Table IV, we present the realisable mass matrix textures and their corresponding Yukawa decompositions. Table V displays, for each texture set, the Abelian symmetry group that realises the set and the associated transformation charges for each field. In all cases, the full texture decomposition is imposed by the $\mathrm{U}(1)_\mathrm{F}$ symmetry alone. The U(1) symmetry does not impose any texture zero on the mass matrices, but restricts the Yukawa Lagrangian to the form given in Eq. (18), where the term with $\mathbf{Y}^2_R$ is forbidden and $\mathbf{Y}_R \equiv \mathbf{Y}^1_R$. Since for all realisable cases $\mathbf{M}_R$ and $\mathbf{M}_s$ are fixed by the textures T_{14} and T_{23}, respectively, we will refer to each case through the pair notation $(\mathbf{M}_\ell, \mathbf{M}_D)$.

V. LEPTON MASSES, MIXING AND LEPTONIC CPV

Throughout the rest of this work we restrict our phenomenological analysis to the combination $\left(5^\ell_{1,\mathrm{I}}, \mathrm{T}_{45}\right)$. We consider the scenario in which CP is imposed at the Lagrangian level. It can be shown that the scalar potential of the fields Φ and $S_{1,2}$, with specific soft breaking of the $\mathrm{U}(1)\times\mathbb{Z}_2\times\mathrm{U}(1)_\mathrm{F}$ symmetry, allows for a SCPV stemming from the complex phase $e^{i\xi}$ of the VEV of the singlet S_1 (see Ref. [20] for details). The mass matrices are parameterised as

$$\begin{aligned}&\mathbf{M}_\ell = \begin{pmatrix}0&0&a_1\\0&m^2_{\ell_1}&0\\a_2&0&a_4\end{pmatrix}\ ,\ \mathbf{M}_D = \begin{pmatrix}m_{D_1}&m_{D_3}\\m_{D_4}&0\\0&m_{D_2}\end{pmatrix}\ ,\\ &\mathbf{M}_R = \begin{pmatrix}0&M\\qM&0\end{pmatrix}\ ,\mathbf{M}_s = \begin{pmatrix}p\,\mu_s e^{i\xi}&0\\0&\mu_s e^{-i\xi}\end{pmatrix},\end{aligned} \tag{20}$$

where all parameters are real. Note that, the charged-lepton state ℓ_1 is decoupled from the remaining ones, leading to three distinct cases of $5^{\ell_1}_1$ textures with $\ell_1 = e,\mu,\tau$, labelled as $5^{e,\mu,\tau}_1$. The diagonalisation of the charged-lepton mass matrix is performed by the unitary rotations $\mathbf{V}_{L,R}$ with angles $\theta_{L,R}$. Furthermore, p and q are dimensionless rescalings.

It can be shown that the effective mass matrix $\mathbf{M}_{\text{eff}}$ can be written in terms of six relevant effective parameters namely the phase ξ, angle θ_L and

$$\begin{aligned}&x = \mu_s\frac{m^2_{D_4}}{M^2}\ ,\ y = \mu_s\frac{m_{D_1}m_{D_4}}{M^2}\ ,\\ &z = \mu_s\frac{m_{D_2}m_{D_3}}{M^2}\frac{p}{q^2}\ ,\ w = \mu_s\frac{m^2_{D_2}}{M^2}\frac{p}{q^2}\ .\end{aligned} \tag{21}$$

These six parameters are to be compared with seven low-energy physical parameters, namely three mixing angles θ_{ij}, two neutrino masses and two CPV phases, i.e., the Dirac and Majorana phases, δ and α, respectively. Thus, there is a relation among the elements of the effective neutrino mass matrix, which results in a correlation between two low-energy parameters. Moreover, θ_L, ξ and all parameters in Eq. (21) can be expressed in terms of low-energy neutrino observables.

This leads to a dependence of the effective Majorana mass $m_{\beta\beta}$ (Majorana phase α) relevant for neutrinoless double beta decay on δ as displayed in Fig. 1 for the $5^{e,\mu,\tau}_1$ cases for both mass orderings NO and IO. We show the present upper limits on $m_{\beta\beta}$ reported by the KamLAND-Zen [29], GERDA [30], CUORE [31] and EXO-200 [32] collaborations as well as the future sensitivities planned by the projects AMORE II [33], CUPID [34], LEGEND [35], SNO+ I [36], KamLAND2-Zen [29], nEXO [37] and PandaX-III [38]. First, notice

Fields	U(1)	$(5^{\ell}_{1,\mathrm{I}}, \mathrm{T}_{45})$ $\mathbb{Z}_2 \times \mathrm{U}(1)_{\mathrm{F}}$	$(4^{\ell}_{3}, \mathrm{T}_{124})$ $\mathbb{Z}_2 \times \mathrm{U}(1)_{\mathrm{F}}$	$(4^{\ell}_{3}, \mathrm{T}_{456})$ $\mathbb{Z}_2 \times \mathrm{U}(1)_{\mathrm{F}}$	$(4^{\ell}_{3}, \mathrm{T}_{136,\mathrm{I}})$ $\mathbb{Z}_4 \times \mathrm{U}(1)_{\mathrm{F}}$	$(4^{\ell}_{3}, \mathrm{T}_{146,\mathrm{I}})$ $\mathbb{Z}_4 \times \mathrm{U}(1)_{\mathrm{F}}$
Φ_1	0	$(1,1)$	$(0,-5)$	$(1,1)$	$(1,2)$	$(0,1)$
Φ_2	0	$(0,-1)$	$(1,-3)$	$(0,-1)$	$(0,1)$	$(3,0)$
S_1	0	$(0,2)$	$(0,-2)$	$(0,-2)$	$(0,-2)$	$(0,-2)$
S_2	1	$(0,0)$	$(0,0)$	$(1,0)$	$(0,0)$	$(0,0)$
ℓ_{e_L}	1	$(1,0)$	$(0,0)$	$(0,0)$	$(2,0)$	$(2,0)$
ℓ_{μ_L}	1	$(0,2)$	$(1,2)$	$(1,-2)$	$(1,-1)$	$(1,-1)$
ℓ_{τ_L}	1	$(0,-2)$	$(0,4)$	$(0,-4)$	$(0,-2)$	$(0,-2)$
e_R	1	$(1,-3)$	$(0,9)$	$(1,-5)$	$(3,-4)$	$(0,-3)$
μ_R	1	$(0,3)$	$(1,7)$	$(0,-3)$	$(0,-3)$	$(1,-2)$
τ_R	1	$(0,-1)$	$(0,5)$	$(1,-1)$	$(1,-2)$	$(2,-1)$
ν_{R_1}	1	$(0,1)$	$(0,-1)$	$(0,-1)$	$(0,-1)$	$(0,-1)$
ν_{R_2}	1	$(1,-1)$	$(1,1)$	$(1,1)$	$(2,1)$	$(2,1)$
s_1	0	$(1,-1)$	$(1,1)$	$(0,1)$	$(2,1)$	$(2,1)$
s_2	0	$(0,1)$	$(0,-1)$	$(1,-1)$	$(0,-1)$	$(0,-1)$

TABLE V. Maximally-restrictive texture sets realisable through an Abelian symmetry group. For each texture pair, we provide the $\mathbb{Z}_n$ charges q_n such that the transformation phases are $e^{2\pi i q_n/n}$. The U(1) and $\mathrm{U}(1)_{\mathrm{F}}$ charges are expressed as multiples of the arbitrary charges q_1 and q_{F}, respectively.

that a future measurement of δ in the intervals $[45°, 135°]$ and $[135°, 225°]$ would exclude the NO_μ and NO_τ cases. Secondly, our results show that $m_{\beta\beta}$ is always below the current bounds. However, several future experiments will be able to probe the whole $m_{\beta\beta}$ for IO neutrino masses. In particular, for the current best-fit values given in Table I, we have $m_{\beta\beta} \simeq 40$ meV, which is on the upper IO region. As usual, future experiments with sensitivities of (1.0 - 4.5) meV will be needed to probe the NO regime.

The seesaw approximation provides analytical insight on the heavy-light mixing properties. We start by diagonalising the effective heavy neutrino mass matrix $\mathbf{M}_{\mathrm{heavy}}$ and obtaining the 4×4 unitary matrix $\mathbf{U}_s$ composed of the angles $\varphi_1 \simeq \varphi_2 \simeq \pi/4$. This leads to two pairs of pseudo-Dirac neutrinos with masses $\tilde{m}_{4,5} \simeq M \mp \mu_s/2$ and $\tilde{m}_{6,7} \simeq qM \mp p\mu_s/2$. The mass differences $\tilde{m}_5 - \tilde{m}_4 = \mu_s$ and $\tilde{m}_7 - \tilde{m}_6 = p\mu_s$ are controlled by the small LNV parameter μ_s. From the matrix $\mathbf{U}_s$ and Eq. (14) we obtain the heavy-light neutrino mixing defined in terms of the matrix $\mathbf{B}$ in Eq. (15). Due to the Abelian symmetries imposed to realise the maximally-restricted textures, the $\mathbf{B}_{\alpha j}$ for distinct lepton flavours are related to each other by low-energy neutrino parameters. Indeed, for the 5^e_1 case

$$\begin{aligned} &\frac{\mathbf{B}_{e4}}{\mathbf{B}_{\mu 4}} \simeq \frac{\mathbf{B}_{e5}}{\mathbf{B}_{\mu 5}} \simeq \frac{x}{y c_L}\,, \quad \frac{\mathbf{B}_{\tau 4}}{\mathbf{B}_{\mu 4}} \simeq \frac{\mathbf{B}_{\tau 5}}{\mathbf{B}_{\mu 5}} \simeq \tan\theta_L\,, \\ &\frac{\mathbf{B}_{\mu 6}}{\mathbf{B}_{\tau 6}} \simeq \frac{\mathbf{B}_{\mu 7}}{\mathbf{B}_{\tau 7}} \simeq \frac{z - w\tan\theta_L}{w + z\tan\theta_L}\,, \quad \mathbf{B}_{e6} \simeq \mathbf{B}_{e7} \simeq 0\,, \end{aligned} \tag{22}$$

where all parameters involved depend on neutrino observables. The corresponding relations for the 5^μ_1 and 5^τ_1 textures are obtained by performing the replacements $(e \leftrightarrow \mu)$ and $(e \leftrightarrow \tau)$, respectively.

Note that the complete analysis, succinctly described in this section, can be found in the thesis (or in Ref. [20]).

VI. RADIATIVE CORRECTIONS TO NEUTRINO MASSES

The analysis presented in the previous sections was based on the assumption that the (tree-level) ISS approximation for the neutrino mass matrix given in Eq. (8) is valid, i.e., the parameters in Eq. (20) are such that $\mu_s, m_{D_i} \ll M$. However, the presence of new fermions and scalars may induce relevant radiative corrections to light neutrino neutrino masses [39, 40], denoted $\delta\boldsymbol{\mathcal{M}}$, that should not be overlooked when considering the high precision achieved in the determination of the oscillation parameters, currently at the level of a few per cent for some of those observables (see Table I). For details on the calculation of $\delta\boldsymbol{\mathcal{M}}$ see the thesis (or Ref. [20]).

In our numerical analysis we are interested in:

• Comparing the tree-level light neutrino parameters obtained using the seesaw-approximated $\mathbf{M}_{\mathrm{eff}}$ of Eq. (8) with those stemming from the full neutrino mass matrix $\boldsymbol{\mathcal{M}}$ in Eq. (1). To quantify the effect of considering the ISS approximation at lowest order, we define

$$\Delta_{\mathrm{ISS}} \equiv \frac{|\Delta m^2_{31} - \Delta\tilde{m}^2_{31}|}{\Delta\tilde{m}^2_{31}}\,,\ \Delta\tilde{m}^2_{31} = \tilde{m}^2_3 - \tilde{m}^2_1\,, \tag{23}$$

where the light-neutrino masses m_i and $\tilde{m}_i$ are determined using Eqs. (4) and (9), respectively.

• Evaluating the impact of the one-loop corrections $\delta\boldsymbol{\mathcal{M}}$ on the determination of low-energy neutrino parameters. Likewise the previous case, we define

$$\Delta^{ij}_{\mathrm{1L}} \equiv \frac{|\Delta\widehat{m}^2_{ij} - \Delta m^2_{ij}|}{\Delta m^2_{ij}}\,,\ \Delta\widehat{m}^2_{ij} = \widehat{m}^2_i - \widehat{m}^2_j\,, \tag{24}$$

where $\widehat{m}_i$ are the one-loop corrected neutrino masses and Δm^2_{ij} are the tree-level neutrino mass-squared differences computed with the full $\boldsymbol{\mathcal{M}}$.

For numerical computations in the $5^{e,\mu\tau}_1$ cases discussed in Sections IV and V, we consider a benchmark

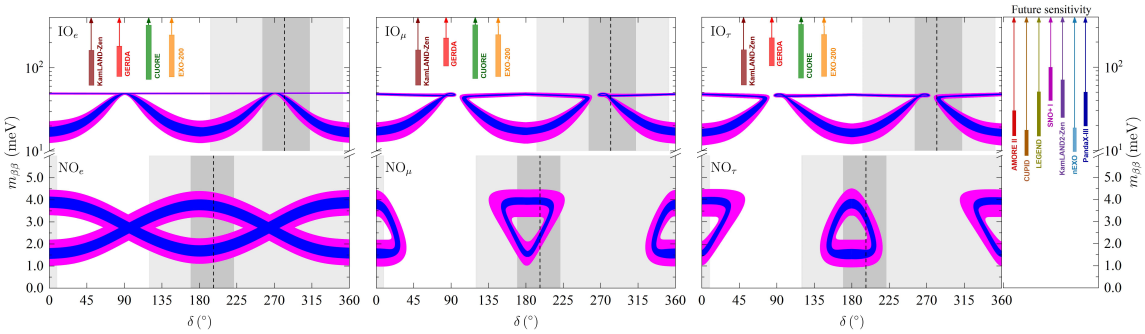

FIG. 1. Effective Majorana mass $m_{\beta\beta}$ as function of the Dirac CPV phase δ for the $5_1^{e,\mu,\tau}$ (left, centre, right) cases. The blue (magenta) regions were obtained taking the 1σ (3σ) intervals for θ_{ij} and $\Delta m^2_{21,31}$ (see Table I). The vertical dark (light) grey band marks the current experimentally allowed region for the phase δ at 1σ (3σ), while the vertical dashed line is at the δ best-fit value (see Table I). In each panel we show the NO and IO results. The current upper bounds on $m_{\beta\beta}$ as well as future sensitivities of numerous experiments (see text for details) are also shown.

scenario based on the following assumptions. We choose $p = 1$ and $q = 10$ in Eq. (20), implying $m_{6,7} \simeq 10\, m_{4,5}$ and $m_5 - m_4 \simeq m_7 - m_6 \simeq \mu_s$. Regarding the scalar sector, we take $\tan\beta = 1$ in Eq. (19) and consider all physical neutral and charged scalar masses to be 1 TeV, except for the SM Higgs boson with mass $m_{H^0} = 125$ GeV. Under these premises we span the parameter space in the following way:

• The low-energy neutrino parameters are fixed to their best-fit values given in Table I, and we compute the effective neutrino mass matrix elements defined in the ISS approximation for both NO and IO neutrino mass spectra. Notice that, the scales m_{D_i}, M and μ_s are not uniquely defined since $\mathbf{M}_{\rm eff}$ is invariant under the rescalings

$$M \to aM \ , \ \mu_s \to b\mu_s \ , \ m_{D_i} \to \frac{a}{\sqrt{b}}\, m_{D_i} \ . \tag{25}$$

In order to probe a wide range of scales, we vary M and μ_s in the intervals $[1, 10^4]$ GeV and $[1, 10^{11}]$ eV. For an arbitrary pair (M, μ_s), we set the rescaling parameters with respect to the initial values, namely $a = M/100$ and $b = \mu_s/10$. The corresponding m_{D_i} are obtained using Eq. (25). Notice that, in order to ensure perturbativity of the Dirac Yukawa couplings b_i we require $y_{\rm max} = \max\{b_{1,2} = m_{D_{1,2}}/v_1, b_{3,4} = m_{D_{3,4}}/v_2\} \leq 5$. We stress that rescaling M, μ_s and m_{D_i} is the only way to probe the parameter space of our model since ratios among different m_{D_i} are determined by the fixed low-energy parameters.

• For each set of (M, μ_s, m_{D_i}), the full 7×7 neutrino mass matrix $\boldsymbol{\mathcal{M}}$ is defined using Eqs. (1) and (20), and then diagonalised as indicated in Eq. (4) to determine $\boldsymbol{\mathcal{U}}$ and m_{1-7}. The active neutrino mixing is characterised by the non-unitary matrix $\mathbf{U}$ of Eq. (13). Finally, we compute the one-loop corrections to the light neutrino masses.

Throughout the remaining of this work, we will use as reference parameters the average mass of the lightest sterile neutrino pair m_{45}, a degeneracy parameter r_N and the mixing of the electron with the lightest sterile neutrino V_{eN}, defined as

$$m_{45} = \frac{m_4 + m_5}{2} \simeq M \ , \ r_N = \frac{m_5 - m_4}{m_{45}} \simeq \frac{\mu_s}{m_{45}} \ , \qquad V_{eN} = |\mathbf{B}_{e4}| \simeq \frac{m_{D_4}}{\sqrt{2}\, m_{45}} \ . \tag{26}$$

In Fig. 2 we show the contour-level plots for $\Delta^{21}_{\rm 1L}$ (left panels) and $\Delta^{32}_{\rm 1L}$ (right panels) defined in Eq. (24) for the NO$_e$ (upper panels) and IO$_e$ (lower panels) cases. From the inspection of these plots we conclude the following:

• The validity of the (tree-level) ISS approximation is verified at less than the percent level for $\mu_s \gtrsim 10 - 20$ eV (region above the $\Delta_{\rm ISS} = 1\%$ horizontal line). The reason why $\Delta_{\rm ISS}$ does not depend on m_{45} for a given μ_s, can be understood taking into account that the next-to-leading-order approximation of the inverse seesaw scales as $\mu_s m_D^4/M^4$ and, consequently, $\Delta_{\rm ISS} \sim m_D^2/M^2 \simeq m_D^2/m_{45}^2$. Thus, if μ_s is kept constant [$b = 1$ in Eq. (25)], m_{D_i} scales as m_{45} leaving $\Delta_{\rm ISS}$ invariant. Moreover, for a given m_{45}, a rescaling of $\mu_s \to b\mu_s$ leads to a rescaling of $\Delta_{\rm ISS} \to \Delta_{\rm ISS}/b$, as can be seen in Fig. 2.

• The chosen intervals for μ_s and M allows us to swipe a wide range for the heavy-light mixing parameter, namely V^2_{eN} lies between 10^{-13} and 10^{-3} in the parameter-space region where the ISS approximation holds up to 1%. The V^2_{eN} contours are approximate horizontal lines since, as shown in Eq. (26), heavy-light mixing scales as m_{D_i}/m_{45} and, consequently, V^2_{eN} remains invariant for constant μ_s due to the same rescaling of m_{D_i} and m_{45}. Notice that this feature fails for $\mu_s \sim m_{45}$ (upper-left corner of the left panels in Fig. 2) since in this case the leading-order ISS approximation for V_{eN} is no longer valid. For the degeneracy parameter r_N, the contours follow the linear relation $r_N \simeq \mu_s/m_{45}$ already shown in Eq. (26) (dash-dotted lines in the right panels of Fig. 2).

• The nearly-vertical levels of $\Delta^{ij}_{\rm 1L}$ indicate that radiative corrections to neutrino masses depend mainly on m_{45}. For NO$_e$, the one-loop corrected Δm^2_{21} deviates from the tree-level result by less than 1% for

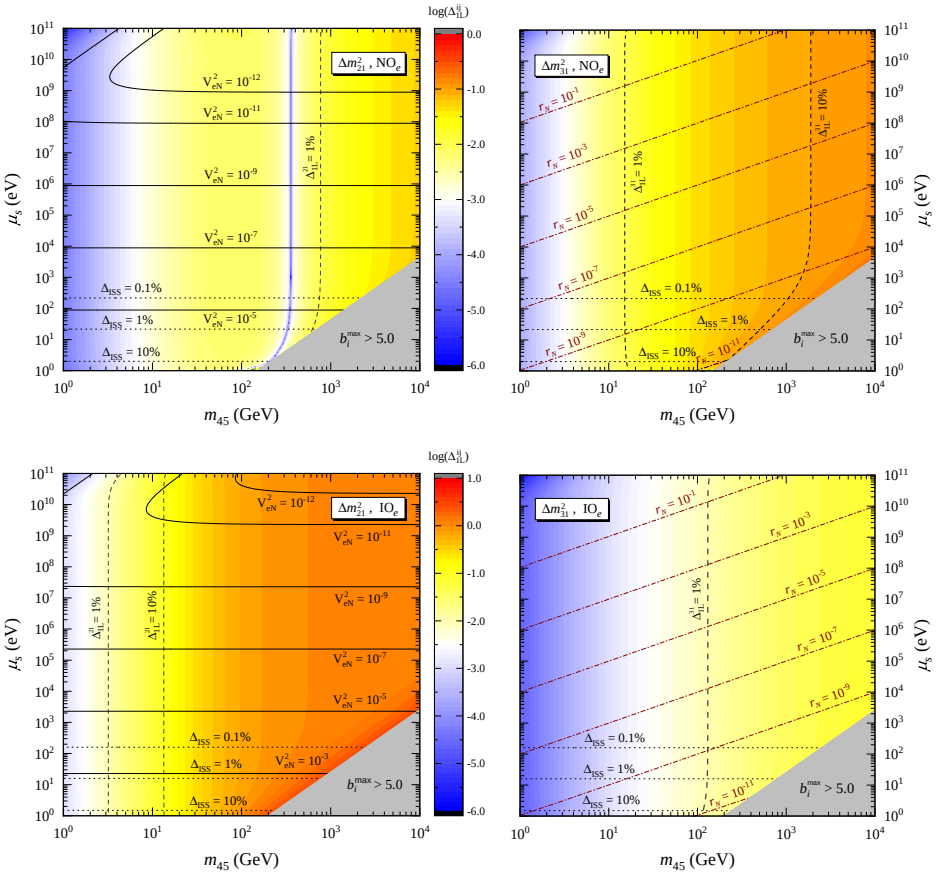

FIG. 2. Impact of one-loop corrections on Δm^2_{21} (left panels) and Δm^2_{31} (right panels) for the NO$_e$ (upper panels) and IO$_e$ (lower panels) cases. The coloured contour levels are for the $\Delta^{ij}_{1\mathrm{L}}$ parameter defined in Eq. (24). For reference, we show the dashed contours with $\Delta^{ij}_{1\mathrm{L}} = 1\%, 10\%$. The solid, dash-dotted and dotted lines correspond to V_{eN}, r_N and Δ_{ISS} contours, respectively. Within the grey shaded region on the lower-right corner of each panel the largest $\mathbf{Y}^{1,2}_D$ obeys $b^{\max}_i > 5$.

$m_{45} \lesssim 700$ GeV, while for Δm^2_{31} that threshold is at $m_{45} \lesssim 20$ GeV. Instead, the corresponding upper limits on m_{45} for IO$_e$ are at 3 GeV and 100 GeV, respectively. In summary, the take-home message to learn from this analysis is that the scale invariance of the tree-level inverse-seesaw approximation holds up to a certain level depending on the sterile neutrino mass.

VII. CHARGED LEPTON FLAVOUR VIOLATION

The ISS model, being a paradigm for low-scale neutrino mass generation, provides a natural scenario for the observation of flavour transitions beyond neutrino oscillations. In the present framework, the symmetries discussed in Section IV provide the ground for a testable scenario in the light of present and future experimental probes on lepton flavour violating (LFV) processes. The results of our numerical analysis are shown in Fig. 3 for the case NO$_e$ (left panel) and IO$_e$ (right panel). The colour codes in the legend of the upper-left panel apply to the whole figure. Our attention is focused on the cLFV processes displayed in this figure, where the present experimental upper limits and future sensitivities for the branching ratios (BR) and conversion rates (CR) (the experiments are mentioned in the text bellow) are shown. By inspecting these results we conclude that:

- The validity of the inverse-seesaw approximation up to 1% level, i.e. $\Delta_{\mathrm{ISS}} < 1\%$, imposes lower bounds on the LNV parameter $\mu_s > 10 - 20$ eV (cyan shaded regions), which correspond to upper bounds on the mixing $V^2_{eN} \lesssim 10^{-4} - 10^{-3}$ (see Fig. 2). The light (dark) grey regions show that a considerable fraction of the parameter space is excluded if one takes into account $b^{\max}_i < 1\,(5)$ as a perturbativity requirement.

- The MEG [41] and SINDRUM II [42] limits on BR($\mu \to e\gamma$) and CR($\mu - e$, Au) exclude $m_{45} \gtrsim 1 - 10$ GeV for $\Delta_{\mathrm{ISS}} \gtrsim 1\%$. Moreover, the improvement on BR($\mu \to e\gamma$) foreseen by MEG II [43] (solid orange contour) would have a marginal impact in covering the parameter space in our framework. On the other hand, reaching a sensitivity of BR($\mu \to 3e$) at the 10^{-16} level (Mu3e [44]) would be more relevant in constraining the parameter space, especially for heavier sterile neutrinos, i.e., for larger m_{45}.

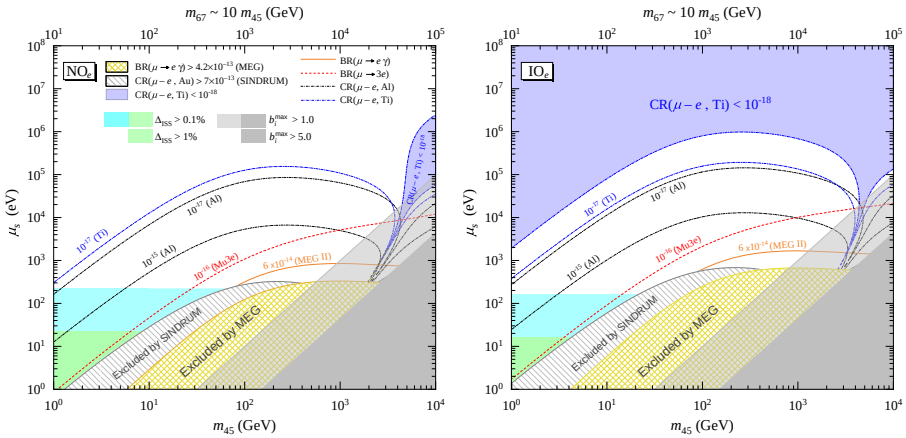

FIG. 3. Constraints on the (m_{45}, μ_s) parameter space imposed by the MEG bound on BR($\mu \to e\gamma$) (yellow crosshatched region) and the SINDRUM II limit on CR($\mu - e$, Au) (grey hatched region). The contours corresponding to the future sensitivities of the MEG II (solid orange) and Mu3e (red dashed) experiments are also given. The black and blue dash-dotted lines show the contours of CR($\mu - e$, Al) and CR($\mu - e$, Ti), respectively, for values within the sensitivity of future experiments (see text for details). In the blue shaded region CR($\mu - e$, Ti) $< 10^{-18}$. Limits on $b_i^{\rm max}$ and $\Delta_{\rm ISS}$ are also shown (grey, green and cyan shaded regions). The results are shown for the 5_1^e case with NO (left panel) and IO (right panel).

• The COMET [45] and PRISM/PRIME [46] projected sensitivities for CR($\mu - e$, Al) and CR($\mu - e$, Ti), represented by black and blue dash-dotted contours, respectively, cover a considerable part of the parameter space, leaving unprobed the regions in shaded blue where CR($\mu - e$, Ti) $< 10^{-18}$. In the best-case scenario NO$_e$, probing CR($\mu - e$, Ti) down to 10^{-18} would cover the whole parameter space, as can be seen in the left panel.

The above results provide a general idea regarding how present experimental data constrain the minimal ISS with Abelian symmetries, and how future experiments would further probe its parameter space. In the thesis (cf. Ref. [20]) we also performed the analysis displayed in Fig. 3 for the remaining NO$_{\mu,\tau}$ and IO$_{\mu,\tau}$ cases. Additionally, we showed that the observation of a particular cLFV decay allows us to draw conclusions regarding others since, due to the Abelian flavour symmetries, the LFV parameters and/or masses are related [see Eq. (22)].

VIII. CONSTRAINTS ON HEAVY STERILE NEUTRINOS AND FUTURE PROSPECTS

In this section we analyse the constraints imposed by cLFV experimental searches on our model, from a perspective where μ_s is replaced by the active-sterile mixing parameters $\mathbf{B}_{\alpha j}$. In our framework, we only need to consider one of these quantities since, as seen in Section V, through Eq. (22), they are all correlated. From now on, we will take as constrained parameters m_{45} and V_{eN}^2 defined in Eq. (26). We will be able to compare the constraining power of the cLFV processes discussed in the previous section with other experimental searches which are usually translated into constraints on mass and mixing parameters. We will consider: **Beam-dump experiments** (Current: NA3 [47] and CHARM [48]; Future: SHIP [49] and DUNE [50]); **High-energy colliders** (Current: L3 [51], DELPHI [52], ATLAS [53, 54] and CMS [55, 56]; Future: HL-LHC [57], FCC-hh [57], FCC-ee [58], ILC [59], CLIC [59], FASER2 [60] and MATHUSLA [61]; Higgs decays [62]; The criterion $R_{ll} \geq 1/3$ to identify the regions of the parameter space where LNV decays are unsuppressed [63, 64]); **Electroweak precision data (EWPD)** (we use the bounds on $\boldsymbol{\eta}_{\alpha\beta}$ from Ref. [65] and we are able thanks to Eqs (15) and (26) to translate them into bounds on $V_{eN}^2 = |\mathbf{B}_{e4}|^2$).

In the left panels of Fig. 4 we present a summary of all the current constraints mentioned above, together with those stemming from $\mu \to e\gamma$ (MEG) and $\mu - e$ conversion in Au (SINDRUM) searches (see Fig. 3), now shown in the (m_{45}, V_{eN}^2) plane. For the EWPD exclusion regions we consider the most restrictive V_{eN}^2 limits extracted from $|\boldsymbol{\eta}_{\mu\mu}|$. On the right, the projected sensitivities of the several experiments enumerated above are shown, including the cLFV ones already presented in Fig. 3 in the (m_{45}, μ_s) plane. For all cases, the overlap of the current exclusion regions (left panels) is shown in light yellow. Looking at the panels we conclude that:

• For $m_{45} \gtrsim 2$ GeV, the strongest constraints are typically those imposed by the SINDRUM and MEG limits on BR($\mu \to e\gamma$) and CR($\mu - e$, Au), respectively, and by EWPD (left panels) for the NO$_e$. However, in the IO$_e$ case, for $2\,\text{GeV} \lesssim m_{45} \lesssim 50$ GeV, the DELPHI, ATLAS and CMS limits are stronger. In both cases, the CHARM exclusion region is more constraining when $m_{45} = 1 - 2$ GeV. Also, the EWPD exclusion regions are not the same for the other NO$_{\mu,\tau}$ and IO$_{\mu,\tau}$ scenarios since the U(1) flavour symmetries, together with present neutrino data, impose different relations among the $\mathbf{B}_{\alpha j}$.

• Any signal of sterile neutrinos with $V_{eN}^2 \gtrsim 10^{-4}$ at future hadron or linear colliders (HL-LHC, FCC-hh,

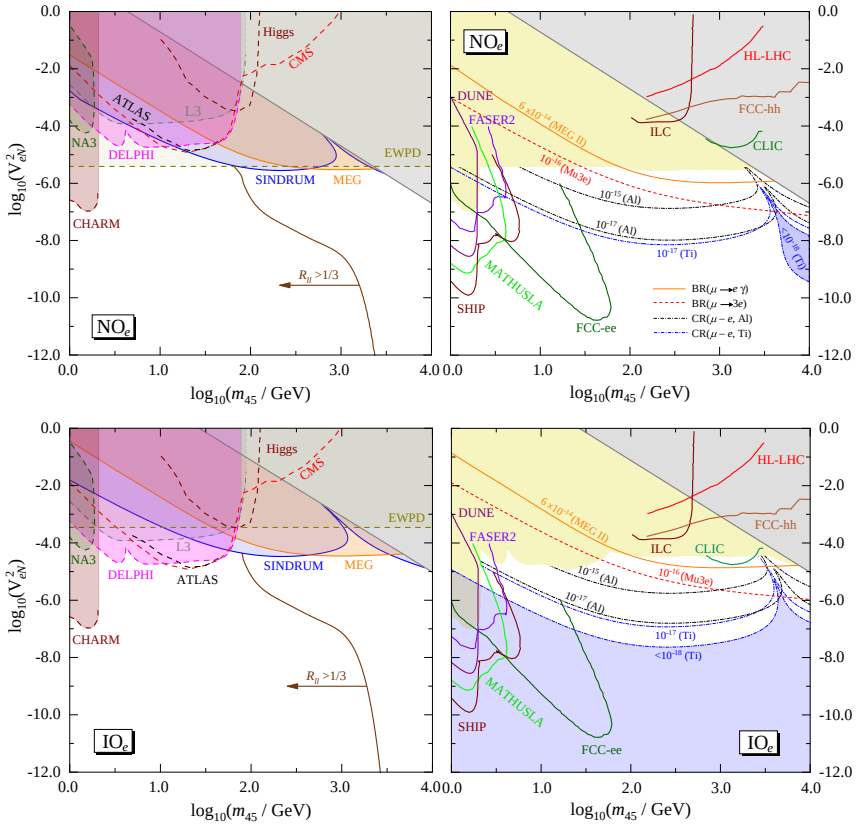

FIG. 4. [Left] Constraints imposed on the (m_{45}, V^2_{eN}) parameter space by the MEG and SINDRUM limits on BR$(\mu \to e\gamma)$ and CR$(\mu - e, \text{Au})$ (see Section VII), by the current searches conducted at colliders and beam-dump experiments and by EWPD (see discussion in the main text). As in Fig. 3, $b_i^{\max} > 5$ within the grey-shaded region. To the left of the solid brown line $R_{ll} > 1/3$. [Right] Projected sensitivities for cLFV searches and other experiments discussed in the text. The yellow-shaded regions correspond to overlapping the current constraints shown on the left panels. Inside the blue shaded region CR$(\mu - e, \text{Ti} < 10^{-18})$. The top (bottom) panels correspond to the NO$_e$ (IO$_e$) case.

CLIC and ILC regions) would not be compatible with the limits already imposed by current constraints from LFV searches and EWPD (see right panels). Therefore, high-energy collider probes conducted at the FCC-ee and at experiments like SHIP, MATHUSLA, DUNE and FASER2 turn out to be of utmost importance.

• For NO$_e$, cLFV indirect searches are fully complementary to the aforementioned direct ones, this is not the case for IO$_e$ nor for the remaining scenarios (see the thesis or Ref. [20] for details). In particular, for inverted neutrino masses, the region with $V^2_{eN} \lesssim 10^{-9} - 10^{-8}$ cannot be probed by future $\mu - e$ conversion experiments. In this case, such mixing regimes can be covered by displaced-vertex experiments and by a high-luminosity Z factory like the FCC-ee. Notice that $R_{ll} \geq 1/3$ within the sensitivity regions of those searches (see the brown solid lines in the left panels), indicating that LNV sterile neutrino decays are not suppressed. It should also be mentioned that in the absence of a positive $\mu \to e\gamma$ signal, the impact of MEG II data would be mild. Instead, if that decay is observed, ranges for m_{45} and V^2_{eN} can be set, being relatively narrow. As for $\mu \to 3e$, future probes conducted by the Mu3e collaboration will be able to cover V^2_{eN} down to $10^{-6} - 10^{-7}$ for wide ranges of sterile neutrino masses.

IX. CONCLUDING REMARKS

We have thoroughly investigated the minimal ISS mechanism with couplings constrained by U(1) flavour symmetries, and with all fermion masses generated via SSB through VEVs of doublet and singlet scalar fields. After finding the maximally-restrictive mass matrices compatible with present neutrino data, we have identified all possible U(1) symmetry realisations and concluded that at least two Higgs doublets and two complex scalar singlets are required to implement those symmetries.

The presence of such singlets opens up the possibility for SCPV, which is successfully communicated to the lepton sector via their couplings to the new sterile fermions. As a result of SCPV and the Abelian symmetries, the low-energy Majorana and Dirac CP phases are correlated. We have also shown that, including one-loop corrections to neutrino masses and requiring them to be at the one percent level, sterile-neutrino mass ranges are

established, within which the tree-level results are still valid in light of the present experimental precision in the determination of the oscillation parameters. Due to the flavour symmetries, the heavy-light mixings are not independent, being their ratios are entirely determined by the lepton observables. This provides a very constrained setup for phenomenological studies.

We have analysed several cLFV decays and obtained the exclusion regions set by the experimental limits on $\mathrm{BR}(\mu \to e\gamma)$ and $\mathrm{CR}(\mu - e, \mathrm{Au})$. These results establish upper bounds on V_{eN}^2 of about $10^{-4} - 10^{-5}$. The prospects to further explore the parameter space were discussed in view of the projected sensitivities of future LFV searches, especially those dedicated to $\mu \to e\gamma$, $\mu \to 3e$ and $\mu - e$ conversion in nuclei.

After analysing the constraining power of cLFV processes, we focused on alternative probes, namely collider and beam-dump experimental searches that are sensitive to sterile neutrinos. We concluded that the HL-LHC, FCC-hh, ILC and CLIC sensitivity regions are already excluded by current LFV and EWPD constraints. On the other hand, searches at a high-luminosity Z factory as the FCC-ee and at experiments like SHIP, MATHUSLA and FASER2 would be highly complementary to the Mu3e, COMET and PRISM/PRIME projects. Hence, it is clear that a single positive signal in any of those experiments would definitely put at test the scenarios studied in this work. In this sense, further symmetry-motivated studies performed in the context of sterile neutrino searches are most welcome.

[1] S. Glashow, *Nucl. Phys.* **22**, 579 (1961).
[2] S. Weinberg, *Phys. Rev. Lett.* **19**, 1264 (1967).
[3] A. Salam, *Conf. Proc. C* **680519**, 367 (1968).
[4] T. Kajita, *Rev. Mod. Phys.* **88**, 030501 (2016).
[5] A. B. McDonald, *Rev. Mod. Phys.* **88**, 030502 (2016).
[6] P. Minkowski, *Phys. Lett. B* **67**, 421 (1977).
[7] M. Gell-Mann, P. Ramond, R. Slansky, *Conf. Proc. C* **790927**, 315 (1979).
[8] T. Yanagida, *Conf. Proc. C* **7902131**, 95 (1979).
[9] J. Schechter, J. Valle, *Phys. Rev. D* **22**, 2227 (1980).
[10] S. Glashow, *NATO Sci. Ser. B* **61**, 687 (1980).
[11] R. N. Mohapatra, G. Senjanovic, *Phys. Rev. Lett.* **44**, 912 (1980).
[12] R. Mohapatra, *Phys. Rev. Lett.* **56**, 561 (1986).
[13] R. Mohapatra, J. Valle, *Phys. Rev. D* **34**, 1642 (1986).
[14] M. Gonzalez-Garcia, J. Valle, *Phys. Lett. B* **216**, 360 (1989).
[15] R. Gonzalez Felipe, H. Serodio, *J. Phys. G* **44**, 065002 (2017).
[16] S. Correia, R. Felipe, F. Joaquim, *Phys. Rev. D* **100**, 115008 (2019).
[17] C. I. Low, R. R. Volkas, *Phys. Rev. D* **68**, 033007 (2003).
[18] G. Branco, *et al.*, *Phys. Rept.* **516**, 1 (2012).
[19] A. Abada, M. Lucente, *Nucl. Phys. B* **885**, 651 (2014).
[20] H. Camara, R. Felipe, F. Joaquim, arXiv:2012.04557 [hep-ph] (2020).
[21] G. 't Hooft, *NATO Sci. Ser. B* **59**, 135 (1980).
[22] W. Grimus, L. Lavoura, *JHEP* **11**, 042 (2000).
[23] W. Rodejohann, J. Valle, *Phys. Rev. D* **84**, 073011 (2011).
[24] P. de Salas, *et al.* (2020).
[25] P. Zyla, *et al.*, *PTEP* **2020**, 083C01 (2020).
[26] P. O. Ludl, W. Grimus, *JHEP* **07**, 090 (2014). [Erratum: JHEP 10, 126 (2014)].
[27] H. Serôdio, *Phys. Rev. D* **88**, 056015 (2013).
[28] I. Ivanov, C. Nishi, *JHEP* **11**, 069 (2013).
[29] A. Gando, *et al.*, *Phys. Rev. Lett.* **117**, 082503 (2016). [Addendum: Phys.Rev.Lett. 117, 109903 (2016)].
[30] M. Agostini, *et al.* (2020).
[31] D. Adams, *et al.*, *Phys. Rev. Lett.* **124**, 122501 (2020).
[32] G. Anton, *et al.*, *Phys. Rev. Lett.* **123**, 161802 (2019).
[33] M. H. Lee, *JINST* **15**, C08010 (2020).
[34] G. Wang, *et al.* (2015).
[35] N. Abgrall, *et al.*, *AIP Conf. Proc.* **1894**, 020027 (2017).
[36] S. Andringa, *et al.*, *Adv. High Energy Phys.* **2016**, 6194250 (2016).
[37] J. Albert, *et al.*, *Phys. Rev. C* **97**, 065503 (2018).
[38] X. Chen, *et al.*, *Sci. China Phys. Mech. Astron.* **60**, 061011 (2017).
[39] A. Pilaftsis, *Z. Phys. C* **55**, 275 (1992).
[40] W. Grimus, L. Lavoura, *Phys. Lett. B* **546**, 86 (2002).
[41] A. Baldini, *et al.*, *Eur. Phys. J. C* **76**, 434 (2016).
[42] W. H. Bertl, *et al.*, *Eur. Phys. J. C* **47**, 337 (2006).
[43] A. Baldini, *et al.*, *Eur. Phys. J. C* **78**, 380 (2018).
[44] A. Blondel, *et al.* (2013).
[45] R. Abramishvili, *et al.*, *PTEP* **2020**, 033C01 (2020).
[46] A. Alekou, *et al.*, *Community Summer Study 2013: Snowmass on the Mississippi* (2013).
[47] J. Badier, *et al.*, *Z. Phys. C* **31**, 21 (1986).
[48] F. Bergsma, *et al.*, *Phys. Lett. B* **166**, 473 (1986).
[49] C. Ahdida, *et al.*, *JHEP* **04**, 077 (2019).
[50] I. Krasnov, *Phys. Rev. D* **100**, 075023 (2019).
[51] O. Adriani, *et al.*, *Phys. Lett. B* **295**, 371 (1992).
[52] P. Abreu, *et al.*, *Z. Phys. C* **74**, 57 (1997). [Erratum: Z.Phys.C 75, 580 (1997)].
[53] G. Aad, *et al.*, *JHEP* **10**, 265 (2019).
[54] G. Aad, *et al.*, *JHEP* **07**, 162 (2015).
[55] A. M. Sirunyan, *et al.*, *Phys. Rev. Lett.* **120**, 221801 (2018).
[56] A. M. Sirunyan, *et al.*, *JHEP* **01**, 122 (2019).
[57] S. Pascoli, R. Ruiz, C. Weiland, *JHEP* **06**, 049 (2019).
[58] A. Blondel, E. Graverini, N. Serra, M. Shaposhnikov, *Nucl. Part. Phys. Proc.* **273-275**, 1883 (2016).
[59] S. Banerjee, P. S. B. Dev, A. Ibarra, T. Mandal, M. Mitra, *Phys. Rev. D* **92**, 075002 (2015).
[60] F. Kling, S. Trojanowski, *Phys. Rev. D* **97**, 095016 (2018).
[61] D. Curtin, *et al.*, *Rept. Prog. Phys.* **82**, 116201 (2019).
[62] A. Das, P. S. B. Dev, C. Kim, *Phys. Rev. D* **95**, 115013 (2017).
[63] M. Drewes, J. Klarić, P. Klose, *JHEP* **19**, 032 (2020).
[64] A. Atre, T. Han, S. Pascoli, B. Zhang, *JHEP* **05**, 030 (2009).
[65] E. Fernandez-Martinez, J. Hernandez-Garcia, J. Lopez-Pavon, *JHEP* **08**, 033 (2016).